Journal of Manufacturing Processes 62 (2021) 720–728

Contents lists available at ScienceDirect

Journal of Manufacturing Processes

journal homepage: www.elsevier.com/locate/manpro

Laser-based additive manufacturing of a binary Ni-5 wt.%Nb alloy

K.C. Atli [a], H.M. Boon [a], R. Seede [a], B. Zhang [b], A. Elwany [b], R. Arroyave [a], I. Karaman [a,*]

[a] Department of Materials Science and Engineering, Texas A&M University, College Station, TX 77843, USA
[b] Wm Michael Barnes '64 Department of Industrial and Systems Engineering, Texas A&M University, College Station, TX 77843, USA

ARTICLE INFO

Keywords:
Laser powder bed fusion
Additive manufacturing
Nickel-based alloys
Selective laser melting

ABSTRACT

In the present study, $Ni_{95}Nb_5$ (wt. %) alloy samples are additively manufactured using selective laser melting (SLM) as a surrogate for Ni-based superalloys. Near porosity-free samples are fabricated utilizing a simple analytical model to predict melt pool dimensions, guide process parameter selection, and determine the defect-free printability map in the process parameter space. $Ni_{95}Nb_5$ mechanical testing specimens displayed consistent yield strengths (~600 MPa) and ultimate tensile strengths (~750 MPa) across a range of process parameters. These results show that with the proper selection of process parameters, SLM can produce parts with consistent mechanical properties in a wide process parameter space in simple alloying systems.

1. Introduction

The field of metal additive manufacturing (AM) has grown substantially over the past few decades, creating many opportunities primarily in the aerospace, defense, and medical device industries [1]. These industries typically feature low production volumes, highly customized parts, and in some cases a large number of components. These characteristics make AM a suitable alternative over traditional manufacturing processes where there is opportunity to eliminate multiple assembly steps, reduce part count, reduce material waste, and improve lead-time for functional end-use parts. However, there are also many challenges associated with AM. For instance, parts are difficult to qualify due to machine-to-machine variability as well as batch-to-batch variability, especially in mechanical properties. Defects, such as porosity, are also a major challenge often seen in final AM parts. Post-processing is typically required to minimize/eliminate the defects stemming from AM, which increases the lead time and cost of the part due to additional processing and labor. Above all, metal AM is limited by the selection of materials that can be successfully processed due to the differences in thermophysical properties of various alloys and their response to non-uniform, often rapid, heating and cooling under commonly used process conditions [2,3].

Recent research and development efforts have focused on designing new materials for AM to meet industry applications [4]. As alloy development for AM continues to evolve, there is a need to accelerate and streamline process optimization whereby process parameters for new materials are determined, and understand the process, structure, and property relationships in new materials fabricated by AM. The conventional method for printing new materials using AM is mostly by trial and error or through lengthy and expensive experimental design such as factorial design. When new materials are printed, it is important to gain an understanding of how the AM process dictates the microstructural evolution and how the microstructure, in turn, affects the mechanical properties of the build. Changing the build parameters of the same material such as laser power, scanning speed, or hatch spacing may lead to a variation in microstructural and mechanical properties since these properties are strongly dependent on the solidification conditions and physical phenomena occurring within the melt pool [5]. For instance, porosity is a common defect in AM processes and there are three main mechanisms by which it can be introduced:

a **Keyhole mode:** Typically, the depth of the molten pool during metal AM processes is controlled by conduction of heat in the underlying solid material. However, at high energy densities (i.e. amount of energy deposited per unit volume or unit area) the melting mechanism changes from conduction to the so-called keyhole mode, resulting from an increased recoil pressure—and melt pool penetration—arising from excessive evaporation [2,6]. If keyholes are unstable and repeatedly form and collapse, they are likely to result in voids that consist of entrapped vapor [7].
b **Entrapped gases in the powder:** Depending on the powder fabrication method, it is likely that some powder particles are hollow with gas trapped inside [2]. These entrapped gases result in pores if they cannot escape the melt pool during printing. Porosity can also result

* Corresponding author.
E-mail address: ikaraman@tamu.edu (I. Karaman).

https://doi.org/10.1016/j.jmapro.2020.12.059
Received 10 February 2020; Received in revised form 12 November 2020; Accepted 27 December 2020
Available online 15 January 2021

from the entrapment of the inert atmosphere gas or the alloy vapors inside the molten pool.

c **Lack of fusion (LOF):** Inadequate penetration of the molten pool into the substrate material or the previously printed layer results in LOF defects [8]. Unlike keyholing or entrapped gas porosity, LOF defects generally follow a geometrical pattern defined by the scanning strategy and are easier to discern. Porosity occurring due to LOF typically has sharp edges, and can have a more significant impact on ductility compared to porosity formed due to gas entrapment [2].

In addition to these porosity generation mechanisms, balling is another defect formation mechanism in metal AM. Balling occurs when single-tracks printed at high scan speeds form molten droplets instead of a continuous molten pool. During laser powder bed fusion (L-PBF) and direct energy deposition (DED) metal AM processes, an increase in the scanning speed results in the elongation of the melt pool. At high enough speeds, the melt pool becomes unstable and may break up into small droplets to maintain uniform capillary pressure due to the Plateau-Rayleigh instability [2]. Balling disrupts the continuity of the single-tracks during fabrication resulting in defective parts with poor surface roughness, porosity, and even delamination [9].

Determining AM process parameters for new materials that will yield fully dense parts with minimal defects is a lengthy and costly process. Fortunately, computer simulations can provide AM operators with practical predictions on a material's response to variations in process parameters, which can aid the parameter selection process [10–12]. The Eagar-Tsai (E-T) analytical model is a simplified heat transfer model that was originally used in the welding community and has shown to be simple and efficient for predicting the melt pool geometries during selective laser melting (SLM) [13–16]. In this study, the E-T model is employed to assist with the selection of processing parameters for a L-PBF metal AM process. The model uses a dimensionless form of a travelling Gaussian heat distribution to determine the shape and dimensions of melt pools, and assumes that the heat source is providing constant energy at a constant speed on an infinite substrate. Some limitations for this model's applicability to AM are that it does not account for heat convection, the presence of metallic powder on the surface of the substrate, and vaporization-based processes such as keyhole mode melting. Nonetheless, the model can predict the melt pool size (length, width, and depth) as well as calculate the associated temperature fields [14,17]. One of the goals of the present study is to use this model to define a range of laser power (P) and scanning speed (v) parameters that will enable printing of parts with minimal defects and thereby reduce the number of trial and error runs. The output of melt pool size can then be used to develop design of experiments to determine a range of process parameters to test with single-track experiments. The output of temperature fields is useful for determining how much of the melt pool reaches boiling temperature since significant boiling will lead to the evaporation of elements and undesirable/uncontrolled material properties. The advantage of using the E-T model is that it is computationally inexpensive and many simulations can be run in a relatively short amount of time. Furthermore, it is an analytical model that does not necessitate the use of proprietary codes that might not be accessible to all users.

This study investigates the process, structure, and property relationships in a Ni-5 wt.%Nb alloy, as a model material system, fabricated with selective laser melting (SLM). $NiNb_5$ can be used as a binary proxy for Ni-based superalloys [18–22], which have attracted significant interest in AM community due to their excellent mechanical properties in harsh environments [20,23]. A focus is set on the solidification phenomenon at the single-track level during the L-PBF process, followed by a discussion on how processing parameters govern the porosity and variability in mechanical properties of the built parts. It is demonstrated that with the proper selection of the process parameters to minimize porosity in a wide process parameter space, it is possible to achieve tensile mechanical properties with minimum variability.

2. Experimental and computational methods

2.1. Materials

Gas atomized $Ni_{95}Nb_5$ (wt. %) powder used in this study was acquired from Nanoval GmbH (Germany). A Cameca SX Five scanning electron microscope (SEM) was used to conduct wavelength dispersive spectroscopy (WDS) on powders and built parts. Ni and Nb contents of the powder were measured as 94.7 (± 0.7) and 5.1 (± 0.1) wt. %, respectively. The average particle size of the powder was reported by the manufacturer as d_{10} = 6.7 μm, d_{50} = 19.8 μm and d_{90} = 43.0 μm where d_{xx} denotes the cumulative size percentile of particles that have diameters equal to the number provided. Back scattered electron microscopy images of the as-received powder, recorded using an FEI Quanta 600 SEM, showed spherical particles (Fig. 1a). Cross sectional images of the powder revealed some porosity within the particles (Fig. 1b).

2.2. Additive manufacturing (AM) experiments

AM experiments were conducted on a 3D Systems ProX 200™ laser powder bed fusion (L-PBF) system, equipped with a fiber laser beam having a Gaussian profile, wavelength $\lambda = 1070$ nm, beam spot size of 70 μm in diameter, and a maximum power of 300 W. The experiments were carried out under a protective atmosphere of industrial grade argon during fabrication.

2.3. Thermal model

The Eagar-Tsai (E-T) analytical model is used in this study primarily to predict the melt pool dimensions and temperature profile. The model requires two sets of inputs: (1) material properties and (2) process parameters. In terms of material properties, the model requires the following thermophysical properties of the powder material: melting temperature, T_m; thermal conductivity, k; specific heat capacity, C, and absorptivity, η as well as the bulk density, ρ. E-T model also requires three process parameters: laser power (P), scanning speed (v), and the size of the laser beam at four standard deviations. T_m and ρ were obtained from the manufacturer as 1703 K and 8909 kg/m^3, respectively, whereas the values for k and C were determined as 70.4 W/mK and 636.2 J/kg.K, respectively by using the rule of mixtures for the weighted averages of Ni (95 %) and Nb (5 %) [24]. The absorptivity value of $NiNb_5$ was approximated from the values reported for pure Ni powder (0.501) measured using a 1 μm light source and a layer thickness of 100 μm [25]. Two sets of information can be extracted as the outputs of the E-T model: the melt pool dimensions (length, width, and depth) and the temperature field of the melt pool, the example of which shown in Fig. 2. The mathematical equations defined in the E-T analytical model can be found in the original paper [13].

2.4. Single-track sampling

The objective of printing single-tracks of $NiNb_5$ is to observe the effects of different processing parameters on the resulting melt pool integrity, quality, and dimensions. Once parameters that yield a continuous melt pool without balling and porosity defects are identified, it is relatively easy to build 3D parts which are simply collection of single-tracks and layers. Based on the melt pool temperature distribution data obtained from the E-T model using the thermophysical properties of the powder, the minimum laser power to apply was calculated as 65 W in order to melt a single layer of powder (30 μm in thickness in the present study), assuming an almost stationary laser beam with the scan speed of 0.0001 mm/s. In other words, 65 W was selected as the lower bound of power used while printing the single-tracks, whereas the upper bound was set at 260 W which was the limit of the available L-PBF system. Scanning speed was varied between 50 and 2500 mm/s, where the former is simply a very slow scanning speed from practical point of

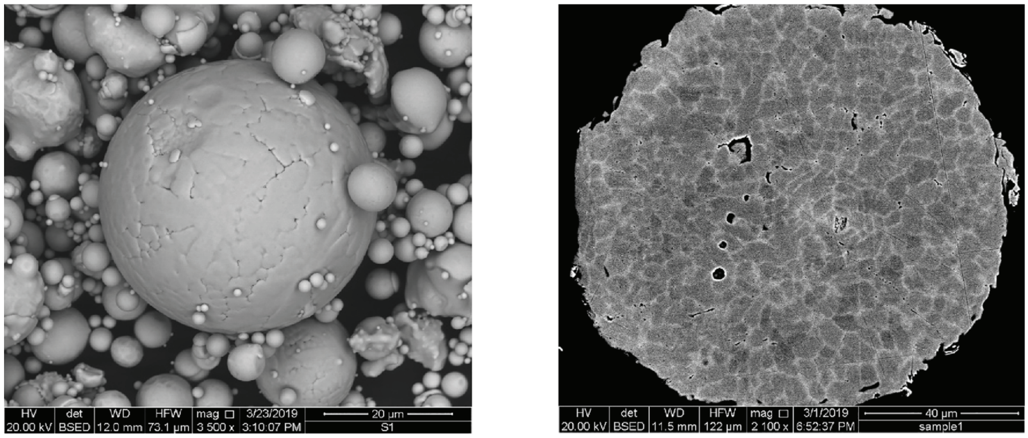

(a) (b)

Fig. 1. Scanning electron microscopy (SEM) back scattered electron (BSE) images of the as-received $NiNb_5$ powder showing a) spherical particles and b) cross-section of a particle with porosity.

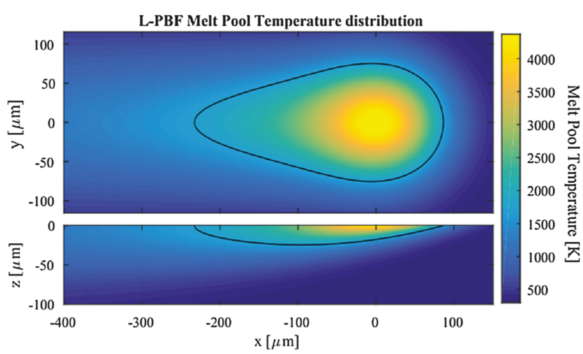

Fig. 2. An example of the Eagar-Tsai model output showing the temperature distribution as well as the dimensions of a melt pool for given set of process parameters, i.e. laser power (P), scanning speed (v), and the size of the laser beam at four standard deviations.

view as it would result in very low build rates, and the latter is the maximum speed the machine allows. With the known thermophysical properties of the $NiNb_5$ powder, a process map with boundary conditions can be established based on the E-T model as shown in Fig. 3. The description for each boundary line that defines a specific porosity formation mode (e.g. keyhole mode and LOF) or physical phenomenon (e.g. melting) is also described in this figure. $D/t = 1$ and $D/t = 1.5$ were chosen as the LOF and optimal track specifications [26,27], respectively, where D is the depth of the melt pool and t is the powder layer thickness. Considering the fact that $D/t = 1$ corresponds to a depth of melt pool just equal to the layer thickness, it is the minimum requirement to yield fusion between successive layers. $D/t = 1.5$ is a more conservative criterion to ensure no LOF. In order to ensure no keyholing porosity occurs in the printed parts, an aspect ratio of $D > W/2.5$ was used, where W stands for the melt pool width. This aspect ratio is more conservative compared to $D/W > 1.5$, which was proposed by Roehling et al. [28]. $T_{max} = T_{melt}$ boundary line corresponds to the condition that the maximum temperature at the melt pool (T_{max}) is equal to the melting temperature (T_{melt}) of the alloy. In other words, below this line, there is no melting at all. Regions I, II and III in Fig. 3 simply represent areas in the P-v process parameter space corresponding to different boundary conditions. For instance, in Region I, the boundary condition is the v value that results in $D/t = 1.5$ at the maximum P of 260 W, based on the E-T model prediction. This region is expected to consist of the feasible process parameters to achieve defect free parts. Similarly for Region II, the boundary condition is the v value that results in $D/t = 1$ at the maximum P of 260 W. Region 3 was bound by the maximum v of the AM system used in this study. In these regions we selected P-v combinations to print single tracks.

It is seen that the optimal range of processing parameters is predicted to be confined within the boundaries of Region I (assuming LOF occurs when $D/t < 1.5$) and it is the region of P and v to test single-track experiments in order to validate the melt pool dimensions. A total of 40

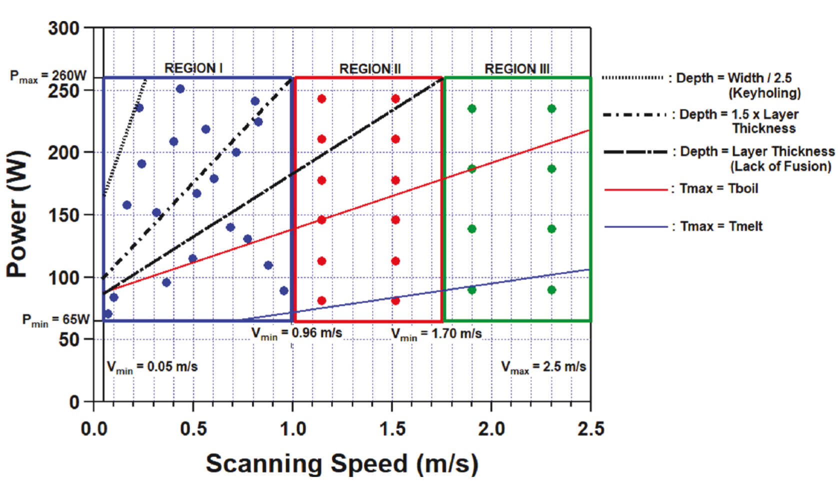

Fig. 3. Power vs. scanning speed process diagram with the boundary conditions for $NiNb_5$ single tracks determined using the E-T model predictions. Boundary conditions were determined using the relative sizes of the melt pool depth, width, and temperature, predicted by the E-T model, and the layer thickness. Refer to the text for details. Data points indicate the power and scan speed combinations selected to experimentally fabricate single tracks using a design of experiment approach once the boundaries are determined.

single-tracks were printed on a Nickel 200 substrate using a layer thickness of 30 μm, which corresponds to the d_{80} value of the powder used. The tracks were printed both inside and outside of Region I to determine if the parameters would in fact fail (i.e., produce keyholing or LOF) according to the boundary conditions. For Region I, a Latin Hypercube Sampling (LHS) method was conducted to produce 20 P and v combinations in a near-random fashion. For Regions II and III, 12 and 8 evenly spaced points were selected, respectively.

Following printing, single-track top views were imaged using an FEI Quanta 600 SEM. Each single-track was cut into three cross-sections using wire electrical discharge machining (EDM). The cross sections of each track were mounted in epoxy, polished to 0.25 μm and finally etched in Kalling's Solution #2 (5 g $CuCl_2$, 100 mL ethanol, 100 mL HCl). Optical microscopy was conducted with a Keyence VH-X digital microscope to measure the melt pool dimensions and compare to the values predicted by the E-T model, as well as characterize any process defects such as LOF, keyholing and balling.

2.5. Printing of cube samples

Once process parameters were selected based on the predictions of the E-T model and empirical boundary conditions that avoid defect formation mechanisms such as keyholing within the melt pool, balling or LOF, cubes with a side length of 10 mm were printed using a bi-directional scanning strategy with a hatch angle of 45°. An additional parameter to consider when building 3D parts is the hatch spacing (h). Hatch spacing is defined as the distance between two adjacent tracks and controls the extent of melt pool overlap. Successful selection of h will result in fusion between adjacent tracks. The number of times a material is remelted and reheated should also be taken into consideration during printing. The greater the h value, the fewer times the previous tracks will be remelted and reheated. The more times a material is remelted, the greater the chance of evaporation of constituent elements and the harder to control the composition. While this issue might not be critical for $NiNb_5$ of the current study, it should be taken into consideration during printing of alloys whose physical or mechanical properties are sensitive to composition. Another point to consider is that increased energy input from reduced h can result in spatter of particles and porosity formation in most alloys [29]. On the other hand, a larger h can result in the formation of porosity due to incomplete melting of the powder layer due to reduced overlap between laser passes.

Similar to P and v, h also has theoretical and functional constraints. The theoretical minimum of h is 0, which corresponds to single-track experiments. Assuming a semicircular shape for the melt pool, the theoretical maximum equals the width of the melt pool (W), which would display maximum LOF between melt pools. In functional terms, the selection of h is usually based on the melt pool width [30]. Letenneur et al. [26] reported an optimal ratio of $W/h = 2.5$ to minimize porosity in as-built Inconel 625.

2.6. Density and composition measurements

Density analysis of the cubes was performed using the Archimedes method based on ASTM B962. A qualitative density comparison of the printed cubes was also conducted by capturing backscattered electron (BSE) images from a section cut parallel to the build direction. Compositional analysis was also conducted using wavelength dispersive spectroscopy (WDS) to quantify the loss of elemental constituents during printing. A total of ten points were analyzed from a cross section cut 1 mm away from the top surface of the cubes normal to the build direction.

2.7. Mechanical property characterization

Five rectangular prisms were fabricated with $34 \times 10 \times 11$ mm^3 dimensions using the process parameters that yielded the least porosity values in printed cubes. Similar to the printing of cube samples, rectangular prisms were printed using a bi-directional scanning strategy with a hatch angle of 45°. Dog-bone shaped tensile specimens with gage section dimensions of $8 \times 3 \times 1$ mm^3, and compression specimens with dimensions $8 \times 4 \times 4$ mm^3 were cut from the prisms using wire EDM. Room temperature monotonic loading tests were performed at a nominal strain rate of 5×10^{-4} s^{-1} using a servohydraulic MTS test frame equipped with a 12.7 mm gage length extensometer and 30 kN load cell. Grips equipped with WC platens were utilized to load the compression samples and unload at around 14 % strain before failure, while tension samples were tested until failure.

3. Results and discussion

3.1. Analysis of single-tracks

Fig. 4 shows a plot of the predicted and experimental melt pool widths and depths as a function of linear energy density (LED, which is equal to P/v), using the thermophysical properties of $NiNb_5$ powder. It is clear that melt pool widths are somewhat overpredicted at lower linear energy density (LED) values and underpredicted at LEDs greater than 0.7 J/mm (Fig. 4a). The melt pool depths are slightly underpredicted at low LED values (<0.3 J/mm), and significantly underpredicted at large LED values (>0.3 J/mm) (Fig. 4b). This is likely because the E-T model does not accurately take keyhole mode melting into account. Since keyhole mode melting accelerates the depth of penetration of the laser, actual melt pool depth is larger than predicted depth at high LED. Even though E-T fails to predict melt pool depth at larger LED values, predictions are acceptable in the low LED regime. As will be seen in the following sections, process parameters for printing cube and rectangular prism samples were selected such that LED values mostly stayed in this regime below 0.4 J/mm. Also it should be noted that using statistical approaches it is possible to calibrate the E-T model but this is beyond the scope of this work.

The quality of the printed single-tracks can be classified based on the top views as few selected ones are shown in the SEM images in Fig. 5. When the top views of single-tracks are investigated, a successfully printed track is simply classified as a continuous track which does not exhibit significant variation in width. Tracks #3 and #4 in Fig. 5 are examples of successful tracks. Tracks #1, #2, and #8 are examples of tracks which are continuous but show great variation in width. These are considered to be failed tracks. As described previously, balling is typically observed at high scan speeds. The melt pool becomes unstable and breaks up into small droplets disrupting the continuity of the single-track. Track #7 is an example of a failed track which exhibits the balling defect. It should be noted that due to the unstable weld formation in the failed tracks, the corresponding cross-sections of the melt pools in Fig. 6 should not be considered as representative of the entire track.

Etched single-track cross sections are displayed in Fig. 6. Track #1 is observed to have a melt pool depth of less than 30 μm and is thus classified as a track that would promote LOF. However, tracks #5 and #6 have depths of 72 and 49 μm, respectively. Since these depths are greater than the layer thickness of 30 μm, these could be categorized as good runs that are sufficient for joining successive layers. The widths of those tracks (88 and 77 μm, respectively) are small and close to the depth values. They are likely to result in LOF defects unless a relatively low h value is selected. These tracks also showed some variability in width, with some regions as narrow as 40 μm and as wide as 100 μm. Overall, it was observed that runs with depths less than 30 μm had widths less than 100 μm. In order to stay within a conservative printability region based off the top view of the single-tracks, single-track parameters that yield track widths less than 100 μm are eliminated for printing 3D parts.

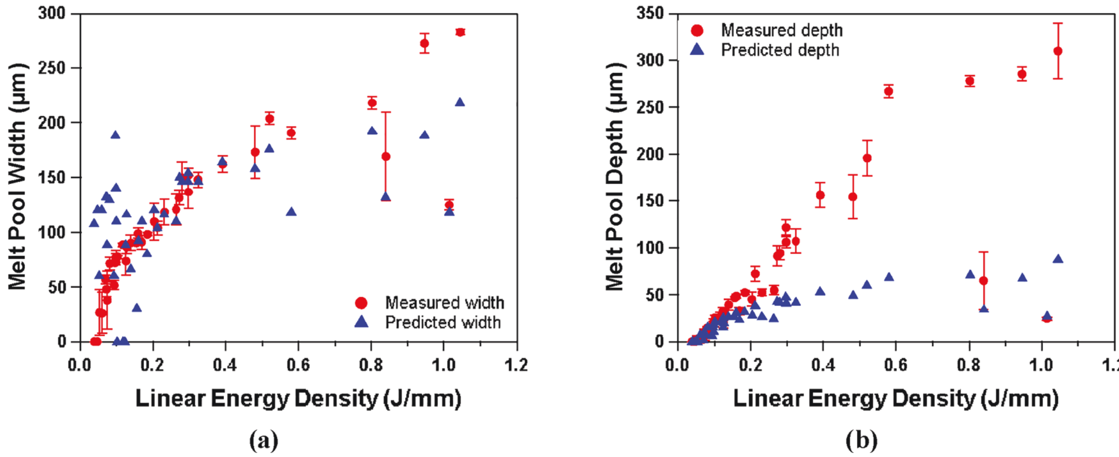

Fig. 4. A comparison of experimental and predicted a) melt pool widths and b) melt pool depth values for the single track experiments for $NiNb_5$ alloy.

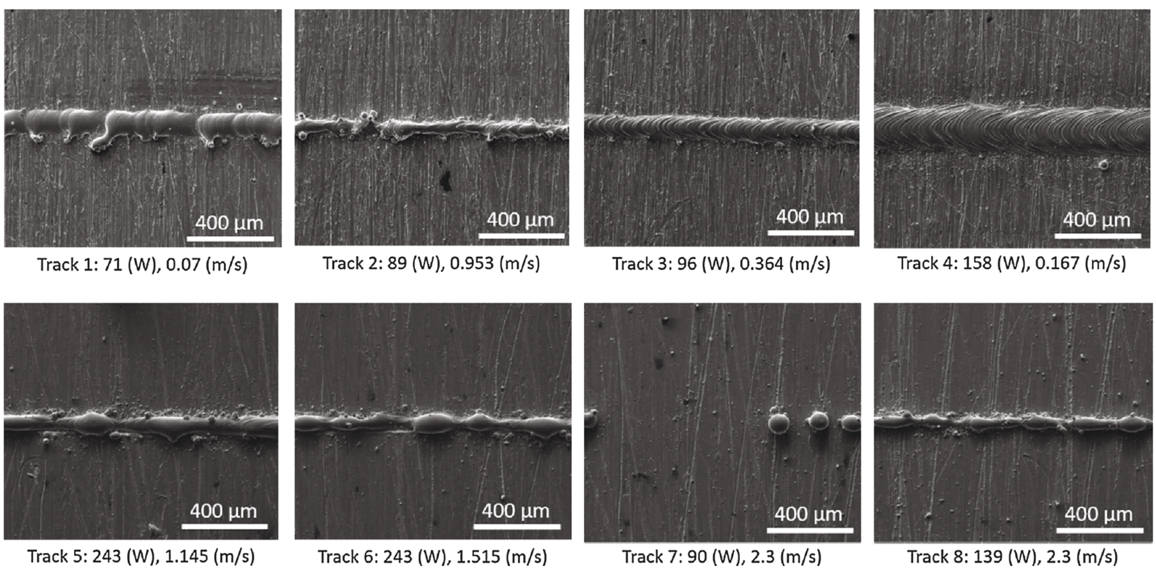

Fig. 5. SEM images showing the top views of some of the selected single tracks of the $NiNb_5$ alloy, which are used to classify successful and failed tracks.

3.2. *Analysis of printed cubes*

Based on the successful single-track parameters, two sets of P and v (250 W, 825 mm/s; 150 W, 495 mm/s) combinations and different *h* values were chosen to print cubes, as listed in Table 1. P and v values were selected from the "printable" region predicted by the E-T model in Fig. 3. In order to determine the optimal *h* values for each of these parameter sets, cubes were printed at 5 different *h* values and the densities for each were measured and compared. For P and v values of 250 W and 825 mm/s, an *h* value of 75 μm resulted in the highest density cube (99.93 % in Cube #2). For values 150 W and 495 mm/s, an *h* value of 85 μm resulted in the highest density (99.74 % in Cube #6). The final build of the cubes is shown in Fig. 7.

Fig. 8 shows SEM images of Cube #1 taken from three different locations on a cross-section cut parallel to build direction. Very little porosity is observed throughout the build. There is a trend of decreasing density in Cubes #6 to #10 as *h* increases. This is likely due to LOF porosity increasing as the tracks are spaced further apart for this P-v parameter set. The melt pool dimensions are too small to fully melt the space between each track at larger *h* values. However, for Cubes #1 to #5 no decreasing trend in density is observed. This indicates larger melt pools that result in full melting between tracks for all *h* values. A summary of the density as a function of *h* for the printed cubes is shown in Fig. 9a. When density is plotted as a function of volumetric energy density (VED), which is simply P/vht, it is seen that, in general, as the VED increased there was a greater tendency for the measured density to be above 99 % (and indeed closer to 100 %), as shown in Fig. 9b. On the other hand, at low VED values (below 80 J/mm^3) densities were consistently below 98 %. Therefore, the VED range of 90 J/mm^3 and above became the region of focus for choosing process parameters to build mechanical testing samples in this study as presented in Section 3.3.

Composition analysis was performed on Cubes #1 to #5 to quantify the loss of Ni during printing as a function of process parameters and volumetric energy density (Fig. 10). All cubes were found to have lost minor amounts of Ni due to the fact that Ni has a higher vapor pressure than Nb at all the relevant temperatures during the melting process [31]. We note that no clear trends were found between Ni loss and *h* or VED, taking into consideration the errors associated with the WDS composition analysis technique, which is ± 1 % of the absolute value measured.

3.3. *Mechanical properties*

Monotonic tensile failure tests were performed at room temperature to characterize the fundamental mechanical properties of the as-printed $NiNb_5$ parts, such as yield strength (YS), ultimate tensile strength (UTS),

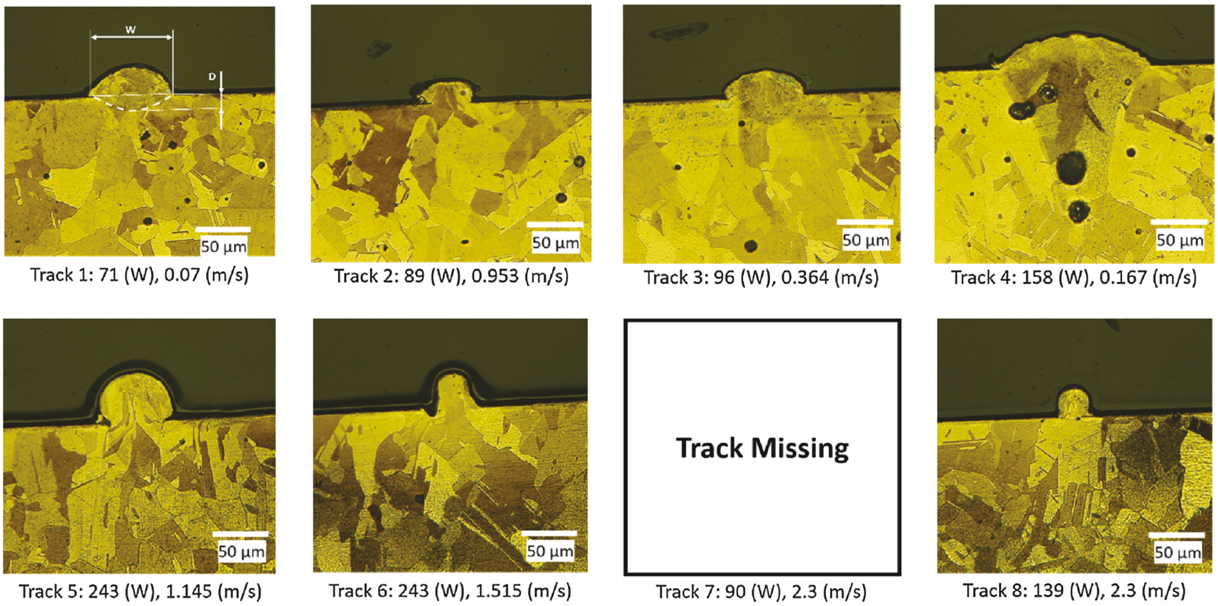

Fig. 6. Optical micrographs of the cross-sections of the selected single tracks of the $NiNb_5$ alloy to evaluate the melt pool depth dimensions, i.e. depth, D and width, W. Track #1 shows a schematic of how D and W measurements are performed.

Table 1
Processing parameters (Power, P; scanning speed, v, and hatch spacing, h) values used to print $NiNb_5$ cubes with resulting linear energy density (LED), volumetric energy density (VED), and measured density values using Archimedes method.

Cube No.	P (W)	v (mm/s)	h (μm)	LED (J/mm)	VED (J/mm^3)	Archimedes Density (%)
1	250	825	60	0.30	168.3	99.756
2	250	825	75	0.30	134.7	99.927
3	250	825	85	0.30	118.8	99.701
4	250	825	105	0.30	96.2	99.762
5	250	825	115	0.30	87.8	99.892
6	150	495	85	0.30	118.8	99.743
7	150	495	120	0.30	84.2	99.376
8	150	495	140	0.30	72.2	97.883
9	150	495	150	0.30	67.3	96.425
10	150	495	155	0.30	65.2	96.376

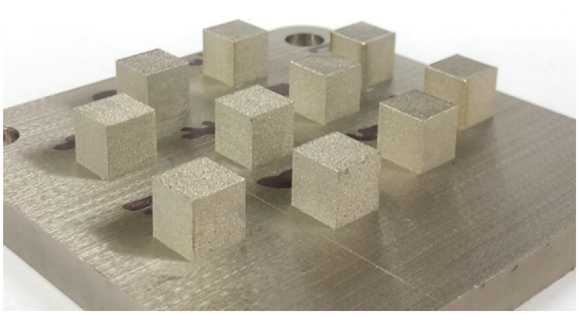

Fig. 7. Set of of the $NiNb_5$ alloy cubes printed using the process parameters listed in Table 1.

and ductility. The first two tensile samples were based on the best two cube prints listed in Table 1 (Cube #6 and #2 for tensile samples 1 and 2, respectively). The remaining three tensile sample parameters (Table 2) were chosen based on the density data plotted as a function of VED (Fig. 9b). The data showed that low porosity builds were in the range of 80–200 J/mm^3. Process parameters yielding VED between 118 and 177 J/mm^3 were chosen for the last three tension samples as listed in Table 2. The single track top and cross-section views corresponding to Samples 2 and 3 are illustrated in Fig. 11a and b, respectively. It is observed that both single tracks are continuous without any LOF and balling defects.

Corresponding stress-strain curves for Samples 1 through 5 are shown in Fig. 12a. Yap et al. [32] reported that L-PBF-processed pure Ni had a UTS of 452.0 $\pm$ 7.4 MPa and a YS of 240.3 $\pm$ 14.0 MPa. It is found in the current study that L-PBF-processed $NiNb_5$ has a higher YS of 595 $\pm$ 15.0 MPa and average UTS of 760 $\pm$ 15.0 MPa than wrought or L-PBF-processed pure Ni. Furthermore, SLM-processed $NiNb_5$ has slightly greater ductility than L-PBF-processed pure Ni [32] due to the latter having higher porosity values with higher chances of crack initiation. The YS of $NiNb_5$ can be predicted to be around 450 MPa through the use of simple calculations based on electronegativity difference of constituent elements [33]. Therefore, the improvements shown in this study for AM $NiNb_5$ can be attributed to the high density of the printed samples, solid-solution strengthening (SSS) with Nb, refined grains and microstructural length scales achieved due to the rapid cooling during L-PBF.

Similar mechanical properties were recorded when samples were tested to failure under compression (Fig. 12b). From these mechanical testing results, it is reasonable to conclude that once near defect free samples are printed with the selection of proper processing parameters, the changes in those parameters are not influential in varying the mechanical properties of the as-printed $NiNb_5$ parts. In addition, the variation in mechanical properties between different samples fabricated using the same AM parameters and those between different porosity free samples fabricated using different AM parameters are minimal, i.e. the properties are quite consistent. Further studies are needed to be able to generalize this conclusion for alloys with similar microstructures, i.e. single phase alloys.

4. Summary and conclusions

A $NiNb_5$ (wt. %) alloy was additively manufactured using laser powder bed fusion additive manufacturing (L-PBF AM) as a surrogate to Ni-based superalloys such as Inconel. The processing parameters used for printing the alloy were selected through the implementation of a simple analytical model. This model was utilized to predict melt pool

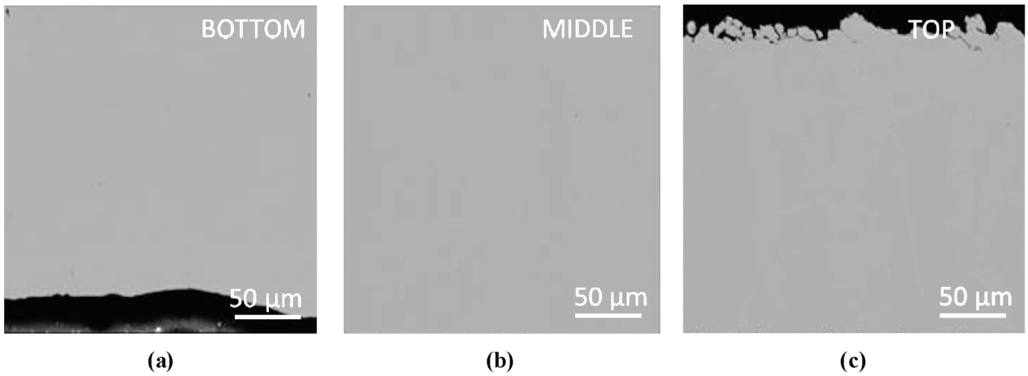

Fig. 8. SEM BSE images for Cube #1 of the $NiNb_5$ alloy taken at three different locations ((a) Bottom, (b) Middle and (c) Top) on a cross-section parallel to the build direction displaying that there is almost no visible porosity in the scale of the images. The cube has a density of 99.756 % as measured by Archimedes' Principle.

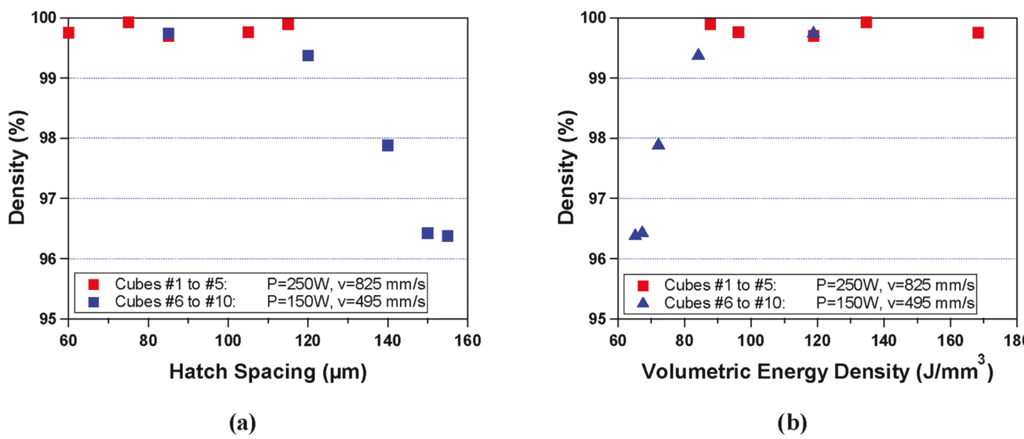

Fig. 9. Density vs. (a) hatch spacing and (b) volumetric energy density (VED) for printed $NiNb_5$ alloy cubes.

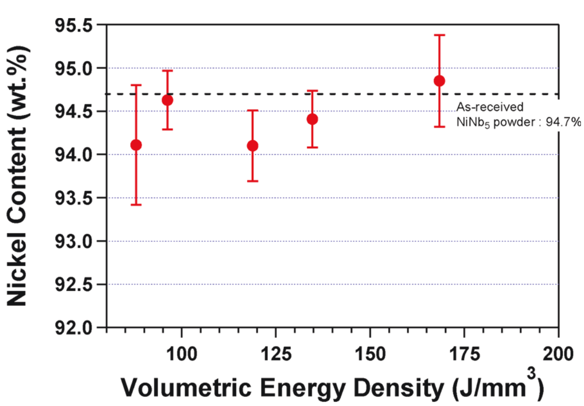

Fig. 10. Matrix Ni-content in printed $NiNb_5$ alloy cubes as measured from the cross-section sliced 1 mm away from the top surface, normal to the build direction.

dimensions and temperatures as a function of laser power and scanning speed. The major findings of the study can be summarized as follows:

1 Higher volumetric energy density (VED) values between 100–200 J/ mm^3 produced the lowest porosity in $NiNb_5$ parts, with densities consistently above 99 %, and in some instances close to 100 %. The change of hatch spacing at this VED range did not have an effect on porosity/density since larger melt pools resulted in full melting of regions between tracks. For VED values below 100 J/ mm^3, porosity increased as hatch spacing increased due to lack-of-fusion defects resulting from poor overlap of melt pools between successive laser passes.
2 Mechanical testing results indicated that as-printed $NiNb_5$ had strength and ductility levels superior to wrought or L-PBF-fabricated pure Ni. The improvements in the mechanical behavior can be attributed to the high density of the printed parts, solid-solution hardening with Nb and refined grain structure induced by L-PBF.
3 It was also seen during mechanical testing that selection of processing parameters, once they were carefully selected to produce

Table 2
Mechanical properties (Tensile yield strength, YS_T; compressive yield strength, YS_C; ultimate tensile strength, UTS; and tensile fracture strain, ε_f of the as-printed $NiNb_5$ tensile and compression testing specimens and the processing parameters used for printing the specimens.

Sample No.	P (W)	v (mm/s)	h (µm)	LED (J/mm)	VED (J/mm^3)	YS_T (MPa)	YS_C (MPa)	UTS (MPa)	ε_f (%)
1	150	495	85	0.30	118.8	610	582	753	13.2
2	250	825	75	0.30	134.7	610	565	773	17.3
3	100	300	70	0.33	158.7	582	558	740	15.7
4	150	550	75	0.27	121.2	591	562	752	14.7
5	200	500	75	0.40	177.8	576	585	771	18.9

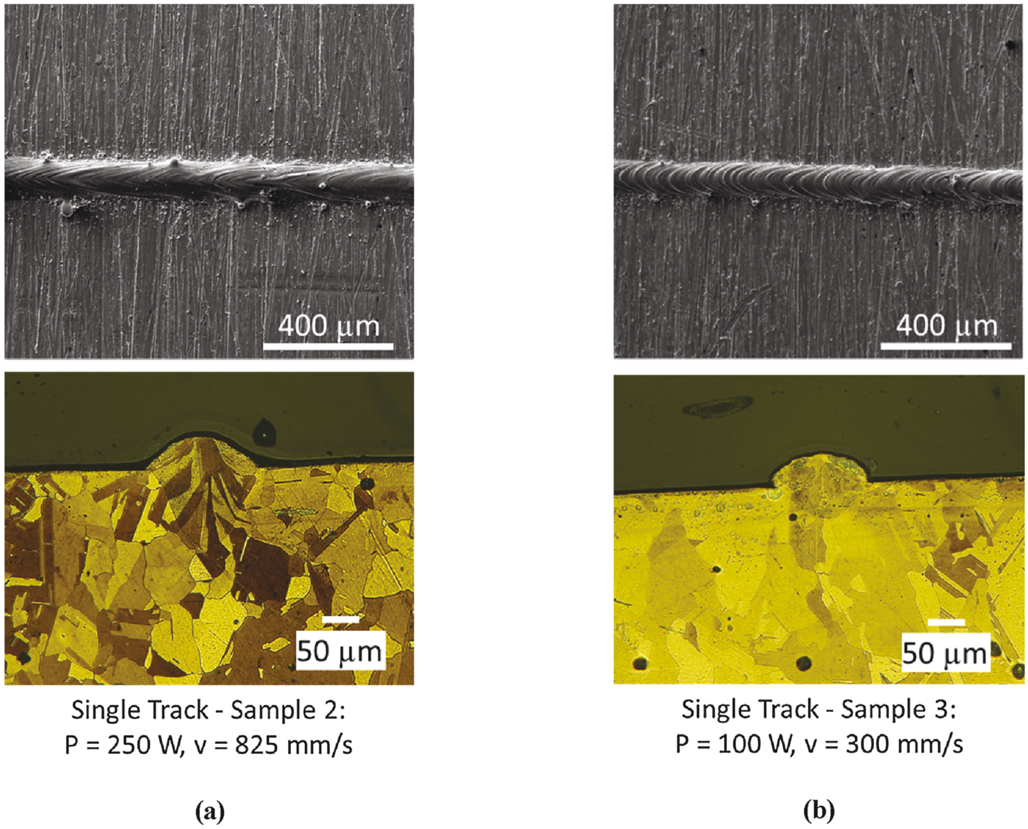

Fig. 11. Top view SEM images and section view optical micrographs of the single tracks that were used for printing rectangular blocks of a) Sample 2 and b) Sample 3.

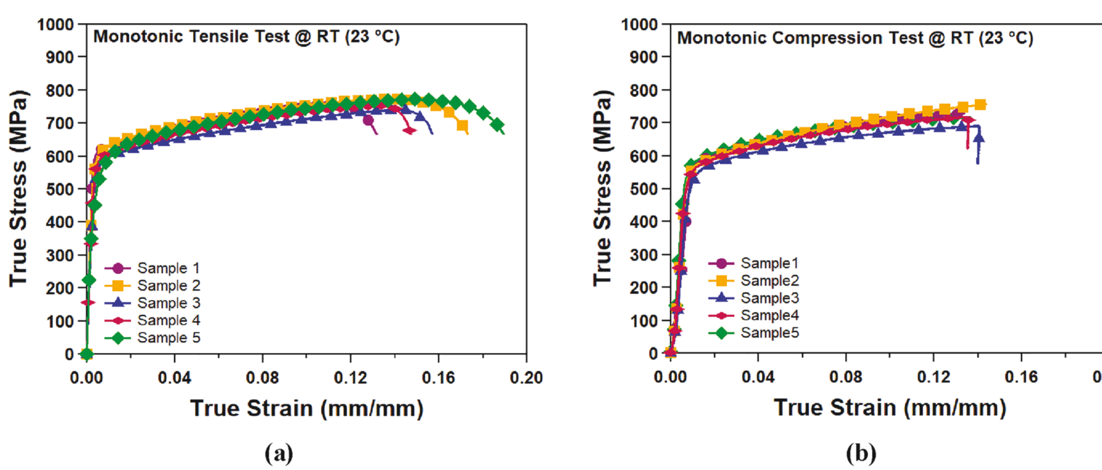

Fig. 12. A comparison of a) tensile and b) compressive stress-strain behavior of the as-printed NiNb5 parts.

near full-density parts, did not result in significant differences in mechanical properties. All printed tensile or compression samples had similar strength values within ±2 % of the average.

Declaration of Competing Interest

The authors report no declarations of interest.

Acknowledgments

The authors acknowledge the support from the Army Research Office (ARO) under Contract No. W911NF-18-1-0278 and the National Science Foundation (NSF) under grant number CMMI- 1846676. The authors wish to thank Dr. Andrew Mott of Texas A&M University, Materials Characterization Facility for the wavelength dispersive spectroscopy analyses.

References

[1] Wohler Associates. Wohlers report 2018: 3D printing and additive manufacturing state of the industry annual worldwide progress report. 2018.
[2] DebRoy T, Wei HL, Zuback JS, Mukherjee T, Elmer JW, Milewski JO, et al. Additive manufacturing of metallic components – process, structure and properties. Prog Mater Sci 2018;92:112–224.
[3] Mukherjee T, Zuback JS, De A, DebRoy T. Printability of alloys for additive manufacturing. Sci Rep 2016;6:19717.

[4] Yap CY, Chua CK, Dong ZL, Liu ZH, Zhang DQ, Loh LE, et al. Review of selective laser melting: materials and applications. Appl Phys Rev 2015;2:041101.
[5] Lippold JC, Kiser SD, DuPont JN. Welding metallurgy and weldability of nickel-base alloys. Wiley; 2009.
[6] Lippold JC. Welding metallurgy and weldability. John Wiley & Sons, Inc.; 2015.
[7] King WE, Barth HD, Castillo VM, Gallegos GF, Gibbs JW, Hahn DE, et al. Observation of keyhole-mode laser melting in laser powder-bed fusion additive manufacturing. J Mater Process Technol 2014;214:2915–25.
[8] Darvish K, Chen ZW, Pasang T. Reducing lack of fusion during selective laser melting of CoCrMo alloy: effect of laser power on geometrical features of tracks. Mater Design 2016;112:357–66.
[9] Li RD, Liu JH, Shi YS, Wang L, Jiang W. Balling behavior of stainless steel and nickel powder during selective laser melting process. Int J Adv Manuf Technol 2012;59:1025–35.
[10] Johnson L, Mahmoudi M, Zhang B, Seede R, Huang X, Maier JT, et al. Assessing printability maps in additive manufacturing of metal alloys. Acta Mater 2019;176: 199–210.
[11] Mahmoudi M, Tapia G, Karayagiz K, Franco B, Ma J, Arróyave R, et al. Multivariate calibration and experimental validation of a 3D finite element thermal model for laser powder-bed fusion metal additive manufacturing. Int eg Mater Manuf Innov 2018.
[12] Karayagiz K, Elwany A, Tapia G, Franco B, Johnson L, Ma J, et al. Numerical and experimental analysis of heat distribution in the laser powder bed fusion of Ti-6Al-4V. IISE Trans 2019;51:136–52.
[13] Eagar TW, Tsai N. Temperature fields produced by traveling distributed heat sources. Weld Res Suppl 1983:346–55.
[14] Kamath C, El-dasher B, Gallegos GF, King WE, Sisto A. Density of additively-manufactured, 316L SS parts using laser powder-bed fusion at powers up to 400 W. Int J Adv Manuf Technol 2014;74:65–78.
[15] Kamath C. Data mining and statistical inference in selective laser melting. Int J Adv Manuf Technol 2016;86:1659–77.
[16] Seede R, Shoukr D, Zhang B, Whitt A, Gibbons S, Flater P, et al. An ultra-high strength martensitic steel fabricated using selective laser melting additive manufacturing: Densification, microstructure, and mechanical properties. Acta Mater 2020;186:199–214.
[17] Wang Y. A processing diagram for high-density Ti-6Al-4V by selective laser melting. Rapid Prototyping J 2018;24:1469–78.
[18] Ghosh S, Ma L, Ofori-Opoku N, Guyer JE. On the primary spacing and microsegregation of cellular dendrites in laser deposited Ni–Nb alloys. Model Simul Mat Sci Eng 2017;25:065002.
[19] Acharya R, Sharon JA, Staroselsky A. Prediction of microstructure in laser powder bed fusion process. Acta Mater 2017;124:360–71.
[20] Amato KN, Gaytan SM, Murr LE, Martinez E, Shindo PW, Hernandez J, et al. Microstructures and mechanical behavior of Inconel 718 fabricated by selective laser melting. Acta Mater 2012;60:2229–39.
[21] Keller T, Lindwall G, Ghosh S, Ma L, Lane BM, Zhang F, et al. Application of finite element, phase-field, and CALPHAD-based methods to additive manufacturing of Ni-based superalloys. Acta Mater 2017;139:244–53.
[22] Ghosh S, Stoudt MR, Levine LE, Guyer JE. Formation of Nb-rich droplets in laser deposited Ni-matrix microstructures. Scr Mater 2018;146:36–40.
[23] Seede R, Mostafa A, Brailovski V, Jahazi M, Medraj M. Microstructural and microhardness evolution from homogenization and hot isostatic pressing on selective laser melted inconel 718: structure, texture, and phases. J Manuf Mater Process 2018;2:30.
[24] Valencia JJ, Quested PN. Thermophysical properties, vol. 15. ASM Handbook; 2008. p. 468–81.
[25] Boley CD, Mitchell SC, Rubenchik AM, Wu SSQ. Metal powder absorptivity: modeling and experiment. Appl Opt 2016;55:6496–500.
[26] Letenneur M, Kreitcberg A, Brailovski V. Optimization of laser powder bed fusion processing using a combination of melt pool modeling and design of experiment approaches: density control. J Manuf Mater Process 2019;3:21.
[27] Yadroitsev I. Factor analysis of selective laser melting process parameters and geometrical characteristics of synthesized single tracks. Rapid Prototyping J 2012; 18:201–8.
[28] Roehling JD, Perron A, Fattebert J-L, Haxhimali T, Guss G, Li TT, et al. Rapid solidification in bulk Ti-Nb alloys by single-track laser melting. JOM 2018;70: 1589–97.
[29] Liu Y, Yang Y, Mai S, Wang D, Song C. Investigation into spatter behavior during selective laser melting of AISI 316L stainless steel powder. Mater Design 2015;87: 797–806.
[30] Letenneur M, Brailovski V, Kreitcberg A, Paserin V, Bailon-Poujol I. Laser powder bed fusion of water-atomized iron-based powders: process optimization. J Manuf Mater Process 2017;1:23.
[31] Yaws CL. Handbook of vapor pressure: volume 4: inorganic compounds and elements. Gulf Professional Publishing; 1995.
[32] Yap Chor Y. Selective laser melting of nickel powder. Rapid Prototyping J 2017;23: 750–7.
[33] Oh HS, Kim SJ, Odbadrakh K, Ryu WH, Yoon KN, Mu S, et al. Engineering atomic-level complexity in high-entropy and complex concentrated alloys. Nat Commun 2019;10(2090).